Evaluation of an Ultra-Wideband Propagation Channel

J.M. Cramer, R.A. Scholtz, M.Z. Win

Abstract— **This paper describes the results of an ultra-wideband (UWB) propagation study in which arrays of propagation measurements were made. After a description of the propagation measurement technique, an approach to the spatial and temporal decomposition of an array of measurements into wavefronts impinging on the receiving array is presented. Based on a modification of the CLEAN algorithm, this approach provides estimates of time-of-arrival, angle of arrival, and waveform shape.**

This technique is applied to 14 arrays of indoor propagation measurements made in an office/laboratory building. Statistical description of the results is presented, based on a clustering model for multipath effects. The parameters of these statistical models are compared to results derived for narrowband signal propagation in the indoor environment.

I. Ultra-Wideband Radio

An ultra-wideband (UWB) radio signal is one whose fractional bandwidth (i.e., its 3 dB bandwidth divided its center frequency) is large, typically over 0.25. Such signals are generated by driving an antenna with very short electrical pulses (on the order of a few nanoseconds to fractions of a nanosecond in duration). Hence these radio systems often are referred to as short-pulse or impulse radio systems. Typically the radiated pulse signals are generated without the use of local oscillators or mixers.

The antennas in UWB systems are significant pulse-shaping filters. In addition, many environments provide a wealth of resolvable multipath. As a result, the received signal often bears little resemblance to the signal driving the transmitter's antenna. If the result of an impulse transmission in free space is a received waveform $p(t)$, then in a typical environment, a typical multipath model for the signal $r(t)$ received over an indoor propagation channel is

$$r(t) \approx \sum_n a_n \, p(t - \tau_n) \,, \tag{1}$$

with a_n and τ_n representing the amplitude and relative delay of the n^{th} component of the received signal. This is a considerably simplified model of reality that is best interpreted as saying that the signal $r(t)$ can be represented as a weighted sum of time-shifted versions of the waveform $p(t)$, without attempting to make strong connections between a_n and τ_n and the physical environment. This model's value is in designing a radio receiver for a digital communication system using modulations constructed from similar pulse sources driving a similar antenna system in a similar environment.

It is more common for a_n and τ_n to be referred to as the amplitude and delay of the n^{th} propagation path, suggesting a more physical interpretation of the environment. This physical interpretation of the channel model is questionable for several reasons. When a wave reflects off an object or penetrates through a material in the process of "multipath" propagation, the effects are frequency sensitive and therefore the waveform is filtered in some way, and the resulting single "multipath component" may actually be represented by several or many terms in the model for $r(t)$. This suggests that a channel model for UWB signals that is more closely related to physical propagation paths should be of the form

$$r(t) \approx \sum_n a_n \, p_n(t - \tau_n) \,, \tag{2}$$

where now the pulse shape associated with a propagation path is dependent on that path. Even more perplexing is the fact that if an antenna is electrically large (e.g., compared to the wavelength of the center frequency of the received signal) the waveforms radiated in different directions from the transmitted antenna look considerably different in the far field [6], and undergo similar direction-dependent distortions on reception. This effect also could be imbedded in a model with path-dependent pulse shape.

A number of propagation studies have been reported, for both indoor and outdoor environments [2], [4], [5], [7], [8], [14], [17], some examining just the temporal properties of the channel and some characterizing the spatio-temporal channel response. The results of these studies may not adequately reflect the special bandwidth-dependent effects associated propagation of UWB signals.

II. An UWB Propagation Experiment

The propagation experiment that we analyze here used two vertically polarized diamond-dipole antennas [9], each 1.65 meters above the floor and 1.05 meters below the ceiling in an office/laboratory environment [21]. The equivalent received pulse at 1 meter in free space can be estimated as the "direct path" signal in an experiment in which there is no multipath signal at small relative delays from the direct path signal. This received waveform, embodying char-

This work was funded in part by the National Science Foundation under Award No. 9730556 and in part by the TRW Space and Electronics Group.

Jean-Marc Cramer is with TRW Space and Electronics, Redondo Beach, CA 90278, USA. E-mail: jean-marc.cramer@trw.com

Robert Scholtz is with the Communication Sciences Institute, EEB 500, Department of Electrical Engineering - Systems, University of Southern California, Los Angeles, CA 90089-2565 USA. E-mail: scholtz@usc.edu

Moe Win is with the Wireless Systems Research Department Newman Springs Laboratory, AT&T Labs-Research, Rm 4-147, 100 Schulz Dr., Red Bank, NJ 07701-7033, USA. E-mail: win@research.att.com

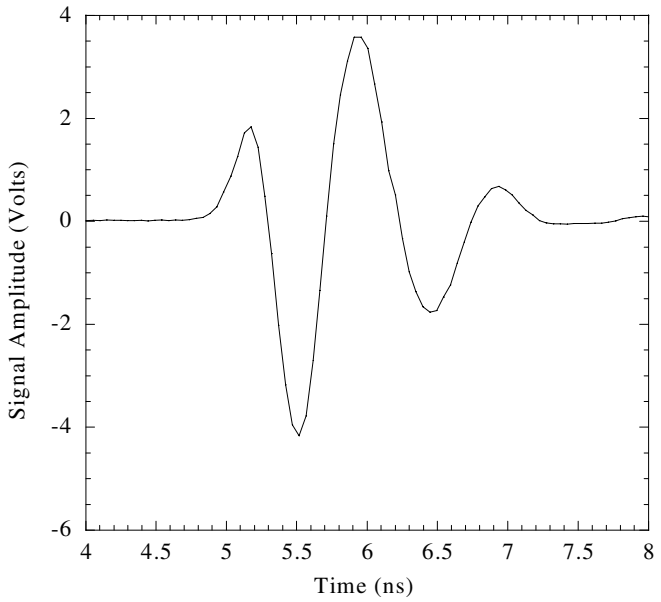

Fig. 1. Transmitted pulse shape captured at 1 meter separation from the transmit antenna

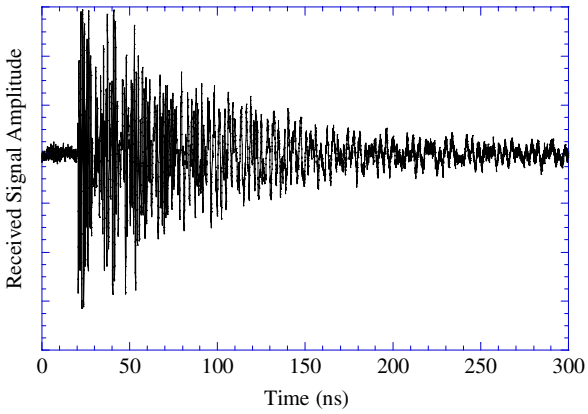

Fig. 2. Received signal on a single sensor at location P

acteristics of the antenna system and pulse driver, is shown in Figure 1.

The placement of the transmitter and various receiving antenna positions are shown on a floor plan in Figure **??**. The building construction is steel stud and dry wall. A typical pulse-induced channel response function is shown in Figure 2. In the experiment, rectangular arrays of measurements are made by moving the receiving antenna to the 49 points in a 7×7 array with 6 inch spacing. Hence each measurement array covers one square yard, and 14 such arrays of measurements are taken at the locations marked on Figure 3. The experimental arrangement included a stable clock that triggered both the receiver (a sampling oscilloscope) and the transmitting pulser. This receiver timing control allowed the sequence of measurements composing the array to be interpreted as simultaneous measurements so that array processing could be used to analyze spatial properties of the received signal. Buried in this approach is the assumption that the environment does not change while the sequence of measurements is being made, and that the receiving antenna support structure, etc., does not significantly affect the measurement. One such array of time-response measurements has been animated and is displayed at `http://ultra.usc.edu/ulab/`.

Several measurement traces and the results of data analysis of individual measurements in this collection (e.g., variations in total trace energy across the array, the effective bit-error rate achieved by an L-tap selective Rake receiver in some array measurement locations as a function of L) are presented in [21].

III. Structure of the CLEAN Algorithm

Our approach to the data analysis uses a variation of the CLEAN algorithm to process arrays of UWB measurements with a minimum of *a priori* information. Initially used to enhance radio astronomical maps of the sky [3], the CLEAN algorithm also has been used in more narrowband communication channel characterization problems [14], [18]

As applied here, the CLEAN algorithm uses delay-and-sum beamforming to construct the beamformer's response as a function of beam direction and time. The beam direction and time giving maximum response are found and a UWB pulse signal is assumed to be present at that time. The only assumption made about the structure of the signal is that it exists within a small window of time at the beamformer output. No canonical wave shape (e.g., the $p(t)$ assumed in (1)) was assumed. Here we develop a directional version of the model in (2) in which different waveform shapes are allowed for different values of n.

We refer to the variant of the CLEAN algorithm used here as the Sensor-CLEAN algorithm, since the relaxation step takes place on the sensor data directly, rather than on the beamformer output. This algorithm is summarized by the following steps.

Sensor-CLEAN Algorithm

1. Input : Digitized pulse response functions in the form of N-tuples from M different sensors; loop gain factor γ (algorithm parameter); the relaxation window half-width $T_{\rm p}$ in samples; a detection threshold $T_{\rm det}$ which is used to control the stopping time of the algorithm; the set of beam pointing angles (azimuth θ_j, elevation ϕ_j), defining the J beampointing directions that discretize the angle of arrival search space.
2. Initialize : Form an MN-dimensional measurement vector $\mathbf{d}(0)$ (the initial residual data vector) by concatenating the N-tuples of waveform time samples for each of M antenna (sensor) positions. Construct the delay-and-sum beamforming matrix $\mathbf{B}$ such that

$$\mathbf{s}(0) = \mathbf{B}\mathbf{d}(0)\,, \tag{3}$$

where the $n+N(j-1)^{\rm th}$ element of $\mathbf{s}(0)$ is the output of the $j^{\rm th}$ beam at sample time n, associated with beamforming at azimuth angle θ_j and elevation angle ϕ_j. (The $JN \times MN$ beamforming matrix $\mathbf{B}$ need only be constructed once.) Set

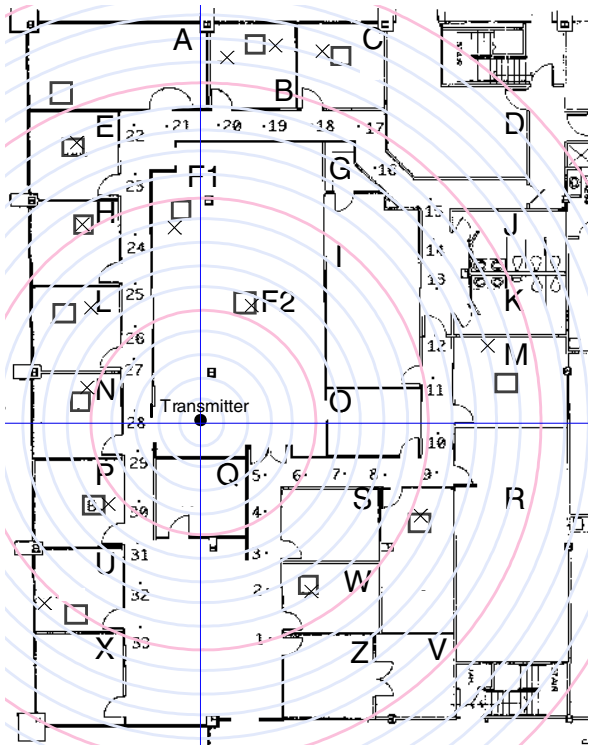

Fig. 3. Measurement floor plan with concentric circles spaced 1 meter apart, centered at transmitter, and measurement array locations indicated by labeled squares. Estimated locations of the measurement sites, determined from the recovered signal information, are indicated by an ×.

the iteration counter i to $i = 0$. Set the detection list $\mathcal{D}$ to the empty list.

3. Signal Detection : Find the index k_{i+1} of the entry which has maximum magnitude in the modified beamformer output $s_k(i)$.

$$k_{i+1} = \text{argmax}_{1 \le k \le JN} |s_k(i)| \,. \tag{4}$$

The entry having maximum magnitude is

$$a_{i+1} = s_{k_{i+1}}(i) \tag{5}$$

If the largest signal is below threshold, i.e., $|a_i| < T_{\text{det}}$, then set the number of iterations $I = i$ and STOP.

4. Increment the iteration counter : $i \rightarrow i + 1$.

5. Window the array data : Form the i^{th} mask vector $\mathbf{b}_i$, an MN dimensional vector to be used to mask the i^{th} residual data vector. The mask $\mathbf{b}_i$ has a 1 in every sensor data position which was used to compute the delay-and-sum beamformer output in the range $s_{k_i - T_{\text{p}}}(i), \ldots, s_{k_i + T_{\text{p}}}(i)$. Mask the residual sensor data to extract the data affecting the i^{th} detected waveform by constructing the MN dimensional vector $\mathbf{b}_i \otimes \mathbf{d}(i-1)$, where $\otimes$ represents the element-by-element multiplication of the two vectors.

6. Residual Beamform : Reduce the residual sensor data vector by a fraction $1 - \gamma$ to produce the residual data vector for the next iteration.

$$\mathbf{d}(i) = \mathbf{d}(i-1) - \gamma\, \mathbf{b}_i \otimes \mathbf{d}(i-1) \tag{6}$$

and regenerate the residual beamformer output

$$\mathbf{s}(i) = \mathbf{B}\mathbf{d}(i) \,. \tag{7}$$

7. Detected signal storage : Append $\{a_i, \theta_i, \phi_i, t_i, \mathbf{w}(i)\}$ to $\mathcal{D}$, where $\mathbf{w}(i)$ is the waveform detected at the beamformer output and removed on the i^{th} iteration,

$$\mathbf{w}(i) = \gamma(0 \ldots, 0, s_{k_i - T_{\text{p}}}(i), \ldots, s_{k_i + T_{\text{p}}}(i), 0, \ldots, 0)^{\text{t}} \tag{8}$$

where $k_i = t_i + [j_i - 1]\, N$ and $0 \le t_i < N$, and θ_i and ϕ_i are the azimuth and elevation angles of beam j_i.

8. Iterate : Go to step 3.

End Sensor-CLEAN

The convergence of the Sensor-CLEAN algorithm is guaranteed through a monotonic reduction in the residual energy on each iteration. As with most indirect algorithms, the solution generated by the Sensor-CLEAN algorithm is not unique; it is a function of the input parameters, in this case γ, T_{p}, and T_{det}, as well as the measured data. The algorithm parameters must be selected based on some criterion which generally trades estimate fidelity against computation time.

Since the precise shape and duration of the received signals is not known a-priori, the Sensor-CLEAN algorithm described above was applied to the measured data multiple times with different relaxation windows, to better match the processing to the anticipated variations in the received signals. Each of these applications results in a list $\{a_i, \theta_i, \phi_i, t_i, \mathbf{w}(i)\}_{i=1}^{I}$ of the amplitude a_i, the azimuth look direction θ_i, the elevation look direction ϕ_i, the time-of-arrival, t_i and the waveform $\mathbf{w}(i)$ recovered on each iteration. A post-processing algorithm also was developed to combine elements of each resulting detection list into a final list of resolvable signal arrivals.

For the results presented below, the beamformer output was generated at 1^o increments in azimuth, and the following nineteen elevations angles are used: 90^o, 88^o, 86^o, 84^o, 82^o, 80^o, 78^o, 76^o, 74^o, 72^o, 70^o, 65^o, 60^o, 55^o, 50^o, 45^o, 40^o, 30^o, 20^o. The three Sensor-CLEAN relaxation windows of $T_p = \pm 6$ samples, $T_p = \pm 8$ samples and $T_p = \pm 12$ samples are used, with $\gamma = 0.10$ and a detection threshold of 0.104 volts. The three relaxation windows and the value of γ were selected to balance algorithm performance and computation time. The detection threshold was chosen to give the algorithms a 30 dB range between the largest and smallest recovered signals at Location P.

IV. Application of Sensor-CLEAN to the Measured Data

The Sensor-CLEAN algorithm and the post-processing algorithms were applied to the measured propagation data. In this section, channel models for UWB signal propagation in an indoor environment are proposed. The primary goal of this effort was to develop models by which quantitative comparisons of the UWB channel with more narrowband indoor propagation results [2], [5], [7], [8], [14] could be made and the performance of UWB communication systems could be predicted. A secondary goal was to use the

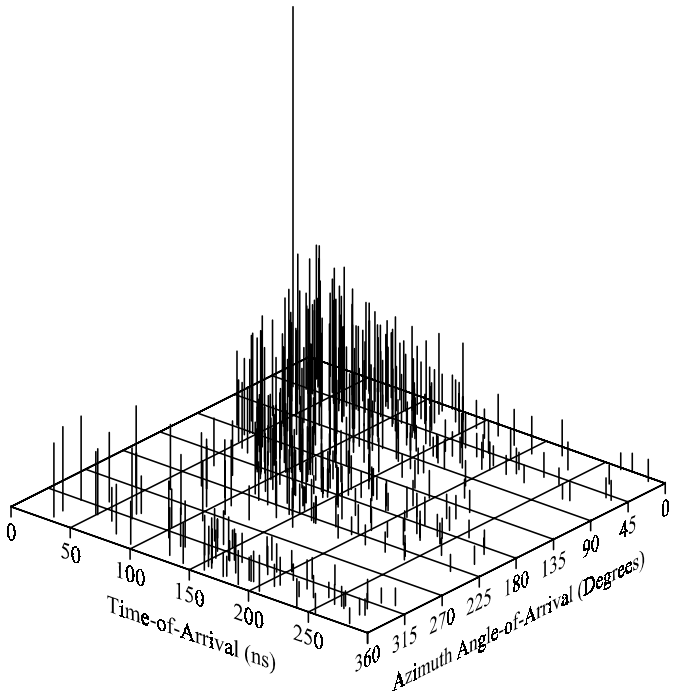

Fig. 4. Recovered signal location and amplitude information at location P.

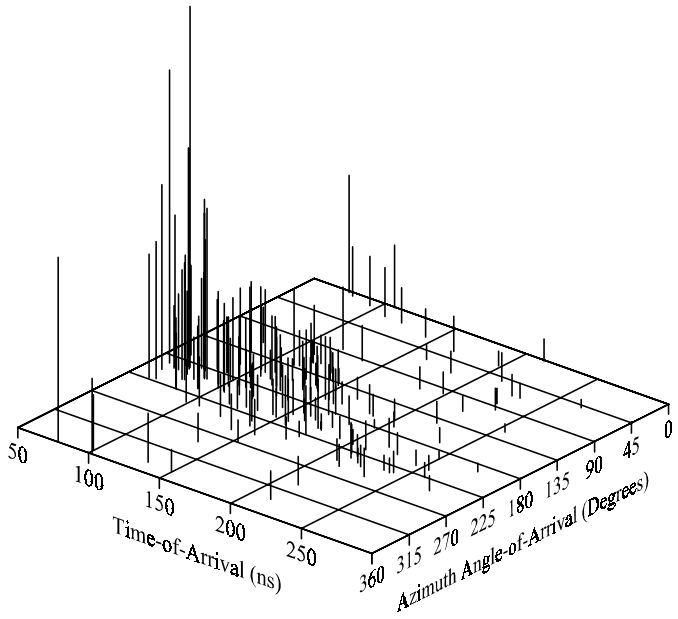

Fig. 5. Recovered signal location and amplitude information at location B.

output of the processing algorithms to study the effects of propagation on the transmitted UWB signals.

The floor plan of the building in which the measurements were made is shown in Figure 3, with the actual location of the measurement arrays indicated by the squares. The recovered measurement locations, indicated by an $\times$ in each room, were determined by the time-of-arrival and azimuth angle-of-arrival of the first incident signal in time recovered by the Sensor-CLEAN and post-processing algorithms. The corresponding direct path length was calculated according to

$$d_{LOS} = (n_1 - n_d) \times c/f_s + 1 \text{ meters} \tag{9}$$

where n_1 is the sample at which the direct-path signal arrives, $n_d = 122$ is the known propagation delay in samples at a 1 meter separation between the transmitter and the receiver, c is the speed of light and f_s is the sampling frequency. With the exception of the result at location A in the building, where the signal strength is weak and the interference is high, the calculated measurement locations correlate reasonably well with the floor plan.

The scatter plots of Figure 4 - Figure 7 display the location of the recovered signal in the time and azimuth plane, and the height of the line is proportional to the amplitude of the recovered signal. Dependence on the elevation angle has been suppressed. In most figures, the existence of clusters of arrivals can be seen, some locations exhibiting a stronger clustering effect than others. These clusters are determined by large scale building features such as the walls, doors and hallways.

The algorithms also recover signal waveform information, and in particular, the direct path waveform recovered at each of the measurement locations was recorded. This gives some insight into the effect of this indoor propagation channel on the transmitted UWB waveforms. For comparison purposes, consider first the signal recorded at a 1 meter separation between the transmitter and the receiver, shown in Figure 1.

Given the transmission of this signal and the processing described above, some of the recovered direct path waveforms are shown below in Figure 8 - Figure 9.

The recovered direct path waveforms are shown in Figure 8 and Figure 9. Each of the waveform plots displays two curves, corresponding to the waveform recovered by the processing algorithms using time windows of different sizes. A larger window has the advantage of giving a more complete picture of isolated signals, while a smaller window may be more successful in resolving dense multipath. Note that there is a progressive distortion of the signal when viewed at 1 meter (Figure 1), shadowed in the same room (Figure 9) and through walls (Figure 8).

V. Clustering Models for the Indoor Multipath Propagation Channel

Previous models for the indoor multipath propagation channel [2], [5], [8], [14], [15] have reported a clustering of multipath components, in both time and angle. In the model presented in [14], the received signal amplitude, β_{kl}, is a Rayleigh distributed random variable with a mean-square value that obeys a double exponential decay law, according to

$$\overline{\beta_{kl}^2} = \overline{\beta^2\,(0,0)} e^{-T_l/\Gamma} e^{-\tau_{kl}/\gamma} \tag{10}$$

where $\overline{\beta^2\,(0,0)}$ describes the average power of the first arrival of the first cluster, T_l represents the arrival time of the l^{th} cluster, and τ_{kl} is the arrival time of the k^{th} arrival

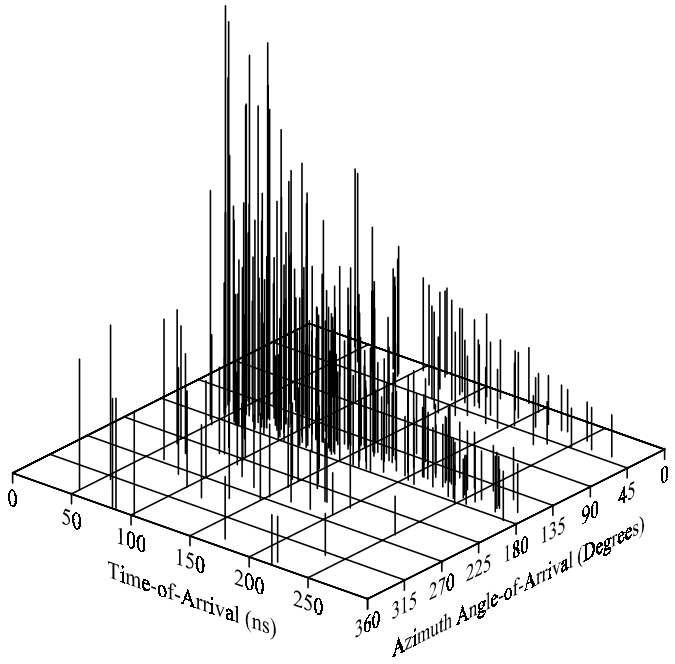

Fig. 6. Recovered signal location and amplitude information at location H.

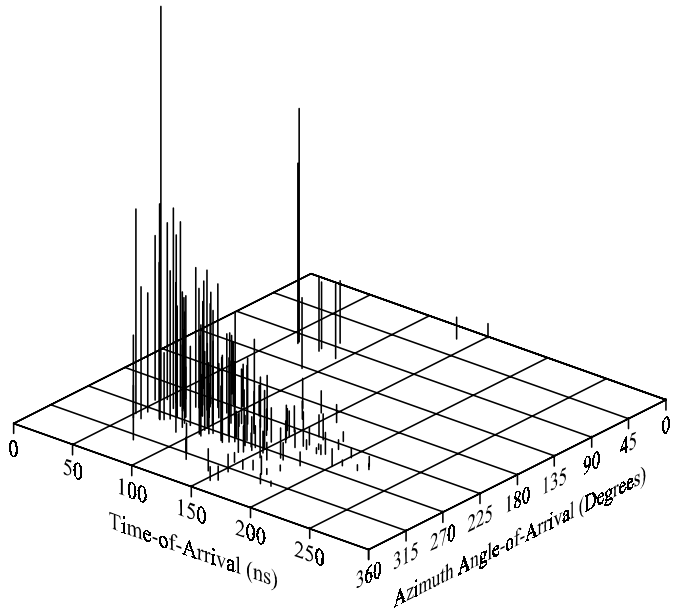

Fig. 7. Recovered signal location and amplitude information at location M.

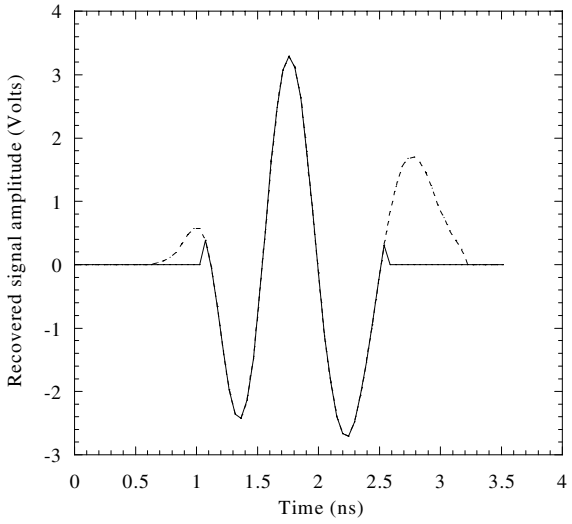

Fig. 8. Recovered direct path waveform at location P.

within the l^{th} cluster, relative to T_l. The parameters Γ and γ determine the inter-cluster signal level rate of decay and the intra-cluster rate of decay, respectively. The parameter Γ is generally determined by the architecture of the building, while γ is determined by objects close to the receiving antenna, such as furniture. The results presented in [14] make the assumption that the channel impulse response as a function of time and azimuth angle is a separable function, or

$$h(t,\theta) = h(t)\,h(\theta) \tag{11}$$

from which independent descriptions of the multipath time-of-arrival and angle-of-arrival are developed. This is justified by observing that the angular deviation of the signal arrivals within a cluster from the cluster mean does not increase as a function of time.

Following this model, and based upon the apparent existence of clusters in the UWB channel seen in Figure 4 - Figure 7, UWB channel models which account for the clustering of multipath components are developed here. As was noted in [14], it is very difficult to develop a robust algorithm for the automatic identification of cluster regions. Here, cluster regions were selected manually by considering both sliding window plots of the arrival density (in time and angle), an example of which is shown in Figure 10, and scatter plots of the time and azimuth angle-of-arrival. In all, 65 clusters were identified in the recovered signals for the fourteen measurement locations.

Following the identification and sorting of the cluster information, the reference arrival, i.e., the earliest arrival in each cluster, was identified, and a decay exponent was determined, again following the methodology in [14]. The time of the first arrival within the cluster is set to zero, and all other arrivals are reported relative to this time. The recovered energy in the collection of signals is also reported relative to the energy in the first arrival in the first cluster, which is normalized to 1, and is referred to as the normalized relative energy, as in [14].

With the measurements at locations A and E excluded because of their low signal-to-noise ratio, the resulting UWB cluster energy versus relative delay models for the indoor channel are shown below in Figure 11 and Figure 12. The first plot reports the decay of the energy in the recovered waveforms, and the second reports the energy as a function of the recovered amplitude only, under the assumption that all incident waveforms are identical. Several values for the decay exponent Γ are shown for each plot, in order to demonstrate the consistency of the results. $\Gamma_{\rm med}$ is the median and $\Gamma_{\rm mean}$ represents the mean of the val-

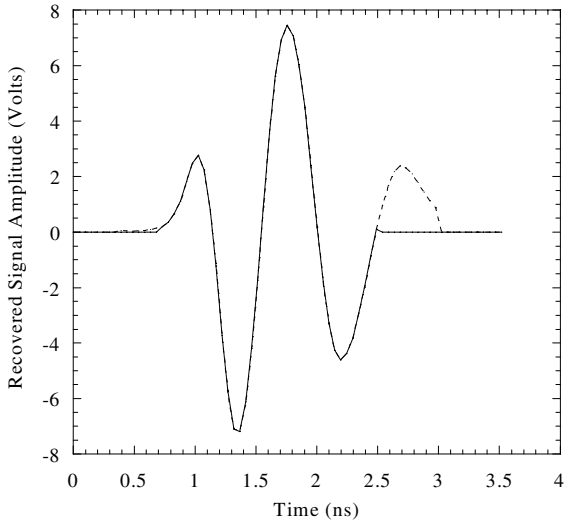

Fig. 9. Recovered direct path waveform at location F2.

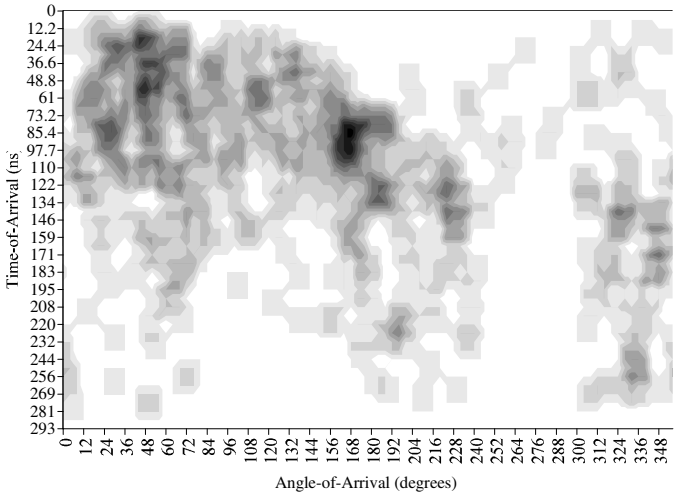

Fig. 10. Density of signal arrivals over time and azimuth angle at location P.

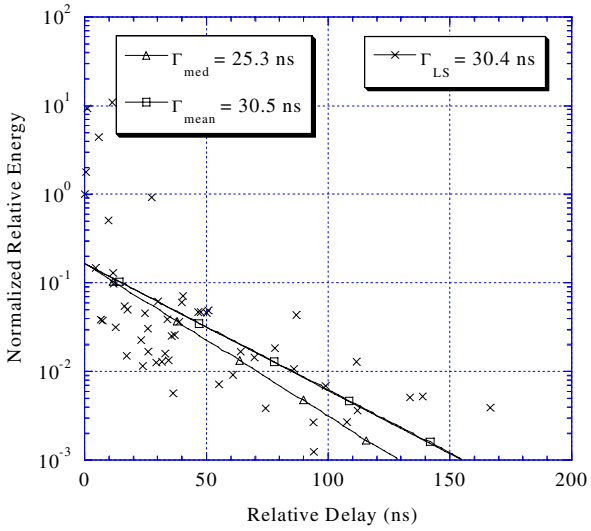

Fig. 11. Inter-cluster loss vs. relative delay when considering the energy in the recovered waveforms (energy of first arrival within a cluster).

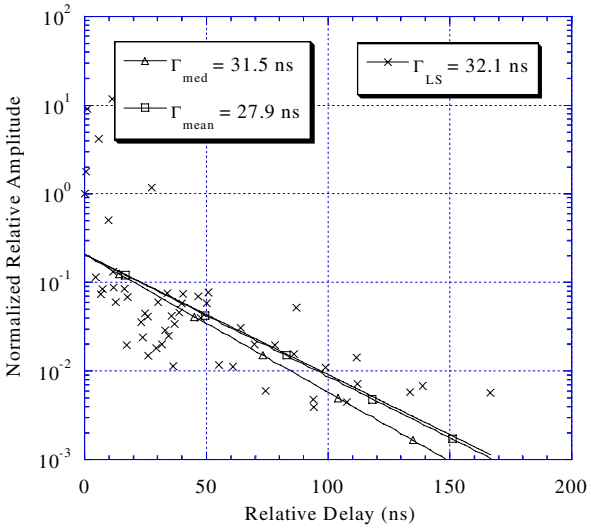

Fig. 12. Inter-cluster loss vs. relative delay when considering the amplitude of the recovered waveforms (amplitude of first arrival within a cluster).

ues obtained by considering the best-fit line for each measurement location individually. Γ_{LS} is the exponent of the best fit line obtained by considering the clusters from all measurement locations simultaneously. In both cases, the results are fairly close, and Γ_{LS} is reported as the rate of decay of the inter-cluster energy versus delay. These results compare to values of 33.6 ns and 78.0 ns reported in [14] for two different buildings, and 60 ns reported in [8]. Thus the UWB signals recovered in this case exhibit a rate of decay that is comparable to some of the results reported previously, although it has been noted that this parameter is a strong function of the building architecture, as are many parameters of the propagation channel. These results allow for comparison against other experiments reported in the literature and for the derivation of a common parameter, the decay exponent, Γ.

Plots of the intra-cluster rate of decay, i.e., the rate at which the recovered energy in individual signal arrivals within a cluster falls off as a function of the delay (also called the ray decay rate [8], [14]) are shown below in Figure 13. The absolute deviation between the mean and median of the results from each measurement location and the least-squares fit to all of the recovered signal information is larger here, excluding the results at locations A and E. The results generated by considering the energy in the recovered waveform and the results from considering the amplitude only are so close that only the former is shown.

In [14], very different results are found for the inter-cluster decay exponent γ, depending on the building in which the measurements were conducted. In one building (cinderblock), a value of 28.6 ns is reported for γ, while in another building (steel frame and gypsum board) γ is found

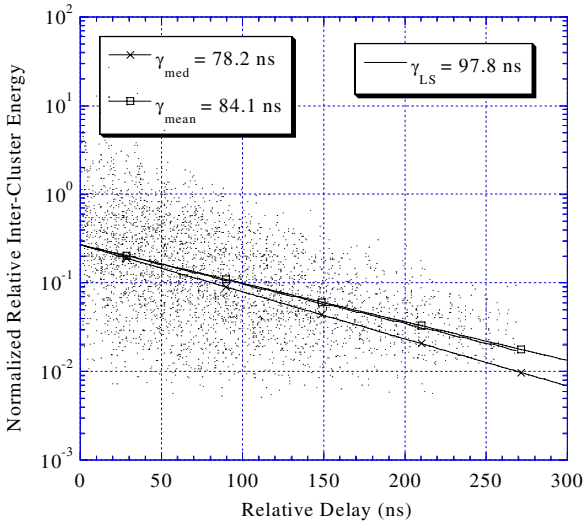

Fig. 13. Intra-cluster loss vs. relative delay when considering the energy in the recovered waveforms.

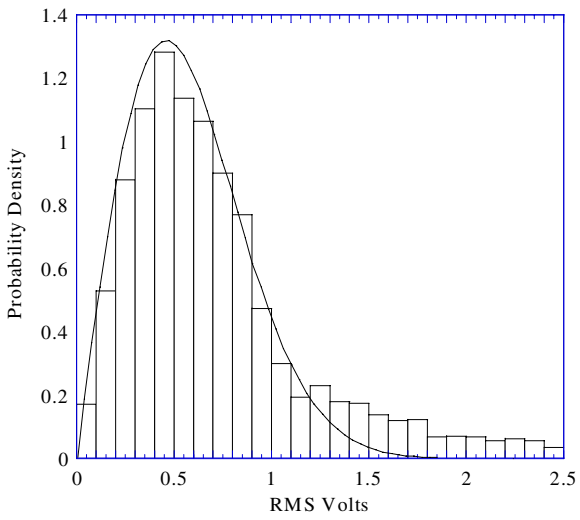

Fig. 14. Distribution of the arrival energy deviation from the mean, with a Rayleigh density overlayed.

to be 82.2 ns. Another reference, [8] reported a γ of 20 ns. The values for γ derived here for the UWB propagation channel are in the same neighborhood as those reported for the steel-frame and gypsum board building in [14].

The cluster decay rate Γ and the ray decay rate γ obtained here can be interpreted for the environment in which the measurements were made. Figure 3 indicates that with the exception of the measurements at locations F1 and F2, at least one wall separates the transmitter and the receiver. Each cluster can be viewed as a path that exists between the transmitter and the receiver along which signals propagate. This cluster path is generally a function of the architecture of the building itself. The component arrivals within a cluster vary because of secondary effects, e.g. reflections off of furniture or other objects. Our interpretation is that the primary source of degradation in the propagation through the features of the building is captured in the decay exponent Γ. Relative effects between paths in the same cluster do not always involve the penetration of additional obstructions or additional reflections, and therefore tend to contribute less to the decay of the component signals.

A Rayleigh distribution has been shown [8], [14] to provide a good fit to the deviation of the arrival energy from the mean curve, where the Rayleigh probability density function is given by

$$f_x(x) = \frac{x}{\alpha^2} e^{-\frac{x^2}{2\alpha^2}}$$

A histogram of the deviation values is shown in Figure 14, with a Rayleigh density with $\alpha = 0.46$ overlaid on top of the recovered distribution. This distribution represents the best-fit to the recovered UWB data when considering the Rayleigh, lognormal, Nakagami-m and Rician distributions as possibilities.

Consider next the angle-of-arrival properties of the cluster model. Assuming again the separable impulse response of equation (11), the model proposed in [14] to describe the angular impulse response is

$$h(\theta) = \sum_{l=0}^{\infty} \sum_{k=0}^{\infty} \beta_{kl} \delta(\theta - \Theta_l - \omega_{kl}) \tag{12}$$

where β_{kl} is the amplitude of the k^{th} arrival in the l^{th} cluster, Θ_l is the mean azimuth angle-of-arrival of the l^{th} cluster and ω_{kl} is the azimuth angle-of -arrival of the k^{th} arrival in the l^{th} cluster, relative to Θ_l. It is proposed in [14] that Θ_l is distributed uniformly in angle, and ω_{kl} is distributed according to a zero-mean Laplacian distribution,

$$p(\theta) = \frac{1}{\sqrt{2}\sigma} e^{-|\sqrt{2}\theta/\sigma|} \tag{13}$$

The recovered rays, i.e., intra-cluster arrivals, were tested against truncated Gaussian and Laplacian densities. It was determined that the relative azimuth arrival angles of the recovered UWB signals were best fit to a Laplacian density, with a standard deviation, σ, of 38^o. The recovered signal information and the best-fit distribution are shown in Figure 15 at 1^o of resolution.

These distributions compare with standard deviations on the Laplacian density of 25.5^o and 21.5^o reported in [14] as the best fit to the recovered angular information for two different buildings. It is likely that this parameter is a function of the building architecture, which again would suggest that further propagation studies are needed to determine whether the results presented here are typical. It is also possible that the difference in the results is due in part to the fractional bandwidth and center frequency of the UWB waveforms used in this study. The penetration properties of these signals, including the larger γ, might lead to the detection of responses that would remain undetected at if transmitted at a single frequency or over a smaller frequency range.

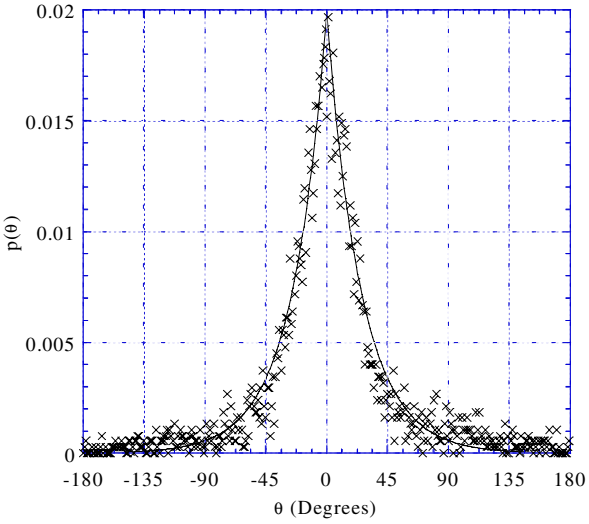

Fig. 15. Ray arrival angles at 1^o of resolution and a best fit Laplacian density with σ=38^o

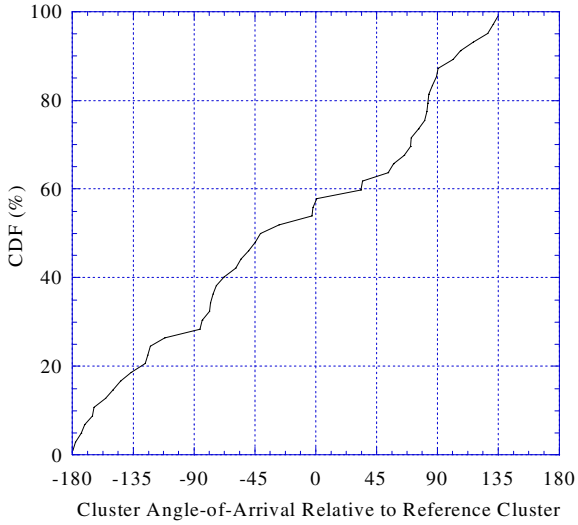

Fig. 16. Distribution of the cluster azimuth angle-of-arrival, relative to the reference cluster.

It was found in [14] that the relative cluster azimuth arrival angles were approximated by a uniform distribution over all angles. The recovered cluster angles in this work are shown in Figure 16, relative to the reference cluster angle-of-arrival, where the reference cluster is taken to be the first cluster to arrive in time, for each measurement location. This distribution is also approximately uniform, although it is noted that no clusters were reported to exist at angles above approximately 135^o. It is conjectured that if more measurements were taken, angles would occur in this region, and this function would tend to more closely approximate a uniform distribution.

Finally, to complete this model of the UWB propagation channel, based on the multipath clustering phenomenon, the rates of the cluster and the ray arrivals must be determined. The inter-arrival times are hypothesized [14] to follow exponential rate laws, given by

$$p\left(T_l \,|T_{l-1}\right) = \Lambda e^{-\Lambda(T_l - T_{l-1})} \tag{14}$$

$$p\left(\tau_{kl} \,|\tau_{k-1,l}\right) = \lambda e^{-\lambda(T_l - T_{l-1})} \tag{15}$$

where Λ is the cluster arrival rate and λ is the ray arrival rate. Following this model, the best fit exponential distributions, parameterized on Λ and λ were determined for the recovered UWB cluster and ray arrival times, respectively. The resulting plots are shown in Figure 17 and Figure 18. The ray arrival rate determined for the UWB signals was faster than that reported in either [14] or [8]. A ray arrival rate of $1/\lambda$=2.3 ns defined the best-fit exponential distribution for the ray arrival times over all measurement locations, while ray arrival rates of $1/\lambda$=5.1 ns and $1/\lambda$=6.6 ns were reported in [14] for the two different buildings. A ray arrival rate of $1/\lambda$=5.0 ns was given in [8]. Several reasons are possible for the faster arrival rate. First, it may be due in part to the building architecture. Second, the fractional bandwidth of the UWB signals and the post-processing algorithms permit multipath time resolution on the order of 1 ns. The measurement equipment used in [14] allowed a time resolution on the incident signals of about 3 ns. Also shown in Figure 17 is a curve which represents the best-fit exponential to ray arrival times of greater than 8 ns, although this represents less than 10% of the values.

A cluster arrival rate of $1/\Lambda$=45.5 ns was found to define the best-fit exponential distribution in the UWB signal propagation model. This value is larger than the cluster arrival rates of 16.8 ns and 17.3 ns reported in [14], but less than the 300 ns given in [8]. Again, several explanations are possible to describe the differences. They could be due to the difference in the fractional bandwidths of the signals involved, the sensitivity of the measurement equipment or the building architecture. As discussed above, they could also be due to the orientation of the transmitter and receiver in the building.

The model parameters derived herein for the UWB signal propagation model and a comparison with the earlier work in [8], [14] are summarized in Table I.

TABLE I
COMPARISON OF CHANNEL MODELS

Parameter	UWB	Spencer et al.	Spencer et al.	Saleh-Valenzuela
Γ	27.9 ns	33.6 ns	78.0 ns	60 ns
γ	84.1 ns	28.6 ns	82.2 ns	20 ns
$1/\Lambda$	45.5 ns	16.8 ns	17.3 ns	300 ns
$1/\lambda$	2.3 ns	5.1 ns	6.6 ns	5 ns
σ	37^{O}	25.5^{O}	21.5^{O}	-

VI. Conclusions

The main goal of this work was to develop an understanding of the indoor UWB propagation channel, including the time-of-arrival, angle-of-arrival and level distributions of a collection of received signals. To accomplish

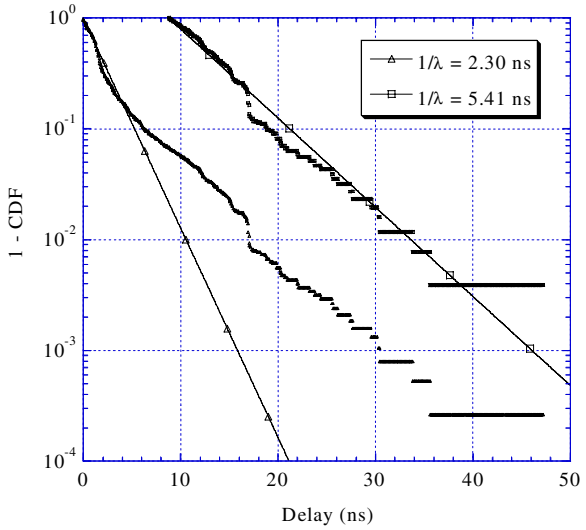

Fig. 17. Ray arrival rate for all measurement locations in the indoor UWB channel considered here.

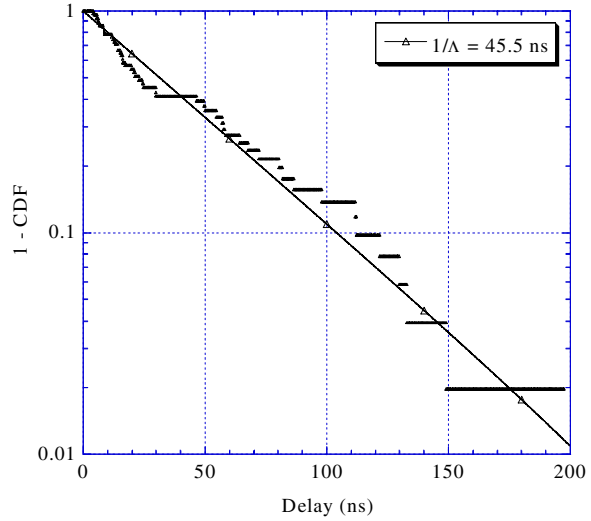

Fig. 18. Cluster arrival rate for all measurement locations in the indoor UWB channel considered here.

this, a set of algorithms suitable for processing UWB signals incident on an array of sensors was developed. These techniques were applied to the measured propagation data. From this, models for the propagation of UWB signals in an indoor channel were generated.

The channel models presented in this work are based on a set of measurement made at a number of locations within an office building. It has been noted that the geometry of the situation and the building architecture can have a significant effect on the received signals [15], [14]. Therefore, further work remains in the collection and processing of propagation data from different buildings,to increase the significance of and augment the results presented in this work. It is possible therefore, that the strongest contribution of this work is in the development of the processing algorithms, and that as more measurements are taken in different environments, the parameters of the UWB channel model presented here will change to reflect this new information.

References

[1] R. J.-M. Cramer, M.Z. Win, R.A. Scholtz, "Evaluation of the Multipath Characteristics of the Impulse Radio Channel," *Proc. of PIMRC '98*, vol. 2, p. 864-868.

[2] H. Hashemi, "The indoor radio propagation channel," *Proc. IEEE*, vol. 81, no. 7, pp. 943-968, July, 1993.

[3] J.A. Högbom, "Aperture Synthesis with a Non-Regular Distribution of Interferometer Baselines," *Astron. and Astrophys. Suppl. Ser.*, vol. 15, p.417-426, 1974.

[4] W. C. Jakes, *Microwave Mobile Communications*, IEEE Press, 1974.

[5] J.C. Liberti and T.S. Rappaport, *Smart Antennas for Wireless Communications: IS-95 and Third Generation CDMA Applications*, Prentice-Hall, Englewood Cliffs, New Jersey, 1999.

[6] J. Maloney et al., "Accurate Computation of the Radiation from Simple Antennas Using the Finite-Difference Time-Domain Method," IEEE Trans. On Antennas and Propagation, July 1990.

[7] D. Parsons, *The Mobile Radio Propagation Channel*, Halsted Press, 1992.

[8] A.A.M. Saleh and R.A. Valenzuela, "A statistical model for indoor multipath propagation", *IEEE JSAC*, vol. 5, no. 2, pp. 128-137, 1987.

[9] H. G. Schantz and L. Fullerton, "The Diamond Dipole: A Gaussian Impulse Antenna," Proceedings of the 2001 IEEE AP-S International Symposium, Boston, July 8-13,2001.

[10] R.A. Scholtz, "Multiple Access with Time-Hopping Impulse Modulation," in *Proc. Milcom*, Oct. 1993.

[11] R.A. Scholtz and M.Z. Win, "Impulse Radio," *Personal Indoor Mobile Radio Conference*, Helsinki, Finland, Sept. 1997, Printed in *Wireless Communications: TDMA vs. CDMA*, S.G. Glisic and P.A. Leppänen, eds., Kluwer Academic Publishers, 1997.

[12] R.A. Scholtz, R. J-M. Cramer, and M.Z. Win, "Evaluation of the Propagation Characteristics of Ultra-Wideband Communication Channels," Antennas and Propagation Society International Symposium, 1998, vol. 2, pp. 626-630.

[13] U.J. Schwarz, "Mathematical-statistical Description of the Iterative Beam Removing Technique (Method CLEAN)," *Astronomy and Astrophysics,* vol. 65, 1978, pp. 345-356.

[14] Q. Spencer, M. Rice, B. Jeffs, M. Jensen, "A Statistical Model for the Angle-of-Arrival in Indoor Multipath Propagation," *IEEE Vehicular Technology Conference*, IEEE, 1997, p. 1415-1419.

[15] Q. Spencer, B. Jeffs, M. Jensen, A. Swindlehurst, "Modeling the Statistical Time and Angle of Arrival Characteristics of an Indoor Multipath Channel," *IEEE Journal on Selected Areas in Communication*, vol. 18, no. 2, March 2000, p. 347-360.

[16] J.D. Taylor, *Introduction to Ultra-Wideband Radar Systems*, CRC Press, Boca Rator, FL, 1995.

[17] G. L. Turin, "Introduction to Spread Spectrum Antimultipath Techniques and their Application to Urban Digital Radio," Proc. IEEE, vol. 68, March 1980, pp. 328-354.

[18] R.G. Vaughan and N.L. Scott, "Super-Resolution of Pulsed Multipath Channels for Delay Spread Characterization," *IEEE Trans. Commun.*, vol. 47, no. 3, March 1999.

[19] M.Z. Win and R.A. Scholtz, "Impulse radio: How it works," *IEEE Commun. Lett.*, Feb. 1998.

[20] M.Z. Win, R.A. Scholtz, M.A. Barnes, "Ultra-Wideband Signal Propagation for Indoor Wireless Communications", *Proc IEEE Int. Conf. on Comm.*, June, 1997.

[21] R.A. Scholtz and M.Z. Win, "Impulse Radio," Personal Indoor Mobile Radio Conference, Helsinki, Finland, Sept. 1997. Printed in ireless Communications: TDMA versus CDMA, S. G. Glisic and p. A. Leppänen, eds., Kluwer Academic Publishers, 1997.